

# OBSERVATIONS OF NEUTRAL BEAM AND ICRF TAIL ION LOSSES DUE TO ALFVÉN MODES IN TFTR

D.S. DARROW, S.J. ZWEBEN, Z. CHANG, C.Z. CHENG, M.D. DIESSO,  
E.D. FREDRICKSON, E. MAZZUCATO, R. NAZIKIAN, C.K. PHILLIPS,  
S. POPOVICHEV\*, M.H. REDI, R.B. WHITE, J.R. WILSON, K.-L. WONG  
Princeton Plasma Physics Laboratory, Princeton University,  
Princeton, New Jersey, United States of America

\* Kurchatov Institute, Russian Research Center,  
Moscow, Russian Federation

**ABSTRACT.** Experimental observations from TFTR of fast ion losses resulting from the toroidicity induced Alfvén eigenmode (TAE) and the Alfvén frequency mode (AFM) are presented. The AFM was driven by neutral beam ions, at low  $B_T$ , and the TAE was excited by hydrogen minority ion cyclotron range of frequencies (ICRF) tail ions at higher  $B_T$ . The measurements indicate that the loss rate varies linearly with the mode amplitude for both modes, and that the fast ion losses during the mode activity can be significant, with tens of per cent of the input power lost in the worst cases.

## 1. INTRODUCTION

### 1.1. Fast ion losses

In a tokamak, knowledge of the rate of fast ion loss is of importance in determining the energy balance of the discharge. Heating of the discharge may be diminished if losses are significant, since neutral beam ions, ion cyclotron range of frequencies (ICRF) heated tail ions and alpha particles all heat the plasma and may all be lost through processes that expel fast ions. In addition, a loss of fast ions that is sufficiently intense and localized may cause damage to plasma facing components in the vacuum vessel of a reactor [1]. For these reasons, a knowledge of the fast ion loss mechanisms is desirable.

Loss processes for fast ions in a tokamak fit into two broad categories: single particle and collective. Single particle loss mechanisms are those, such as first orbit loss, that are independent of the number of fast ions present. These have been seen in numerous instances with various fast ions in TFTR and other tokamaks, and are reported elsewhere [2–7]. Collective losses arise when the fast ion density is sufficient to drive instabilities that then cause loss. The drive can come from  $\partial f_f / \partial \psi$  (where  $f_f$  is the fast ion distribution function) and  $\partial f_f / \partial E$ . Here  $E$  is the particle energy and  $\psi$  is the radial (poloidal flux) co-ordinate. Examples of collective instabilities include the toroidicity induced Alfvén eigenmode (TAE), the kinetic ballooning mode, alpha driven sawteeth, alpha driven fishbones, Alfvén waves and ion cyclotron waves. This paper limits itself to the presentation of observations made during Alfvén

frequency instabilities in TFTR that were excited under two conditions: at low field (1.5 T), with neutral beam ions driving the mode [8, 9], and at intermediate field (3.4 T), with the hydrogen minority ICRF tail ions driving the mode [10–16].

In this paper, we restrict our discussion to experimental measurements of the mode induced fast ion losses. The range of signatures seen in the loss allows some useful inferences to be drawn from the data alone. More could be learned by comparison with the results of numerical modelling. However, lack of knowledge of the plasma current profile, mode radial structure, and, in some cases, mode numbers has prevented us from pursuing simulations.

### 1.2. Detectors

The detectors used to measure the fast ion loss were the ‘escaping alpha’ detectors, which are described elsewhere [2–5, 17, 18]. These detectors act as magnetic spectrometers, dispersing fast ions onto a scintillator, depending upon their gyroradius and pitch angle. The detectors are located at 20, 45, 60 and 90° below the outboard midplane. The probe at 20° below the midplane can be moved in major radius, but the others are fixed in position with their apertures  $\sim 1$  cm behind the limiter. The probes detect fast ions with gyroradii in the range  $2 \text{ cm} \leq \rho \leq 11 \text{ cm}$  and pitch angles in the range  $45^\circ \leq \chi \leq 83^\circ$ , where  $\chi = \cos^{-1}(v_{\text{tor}}/v)$ . The light emitted by fast ion strikes on the scintillators is detected both by an intensified videocamera and by photomultiplier tubes. From the videocamera data, the loss distribution in pitch angle and gyroradius

can be computed, as described and demonstrated in Refs [3] and [4]. The photomultipliers measure the total flux of fast ions to each probe as a function of time, with a much faster sampling rate than is possible with the videocamera.

All the probes, except the 20° probe, have a 3  $\mu\text{m}$  thick aluminium foil over their entrance slit, which stops particles with energies below  $\sim 400$  keV. For this reason only the 20° probe could be utilized in the neutral beam injection (NBI) driven mode studies. For the ICRF tail ion driven TAE, the 20, 45 and 60° probes all showed measurable signals.

### 1.3. Mode characteristics

The TAE is a global mode in a tokamak. It is characterized by a single toroidal mode number,  $n$  ( $n \neq 0$ ), and several poloidal mode numbers,  $m$ , which vary with minor radius. Its frequency is given approximately by  $\omega = v_A/2qR$ , where  $v_A$  is the Alfvén velocity,  $q$  is the local safety factor and  $R$  is the major radius. The mode is driven by the spatial gradient of the fast ion density and, in order for the mode to be unstable, the fast ion velocity must exceed  $v_A$  (although there is some sideband drive of the mode if the fast ion velocity exceeds  $v_A/3$ ). In addition, the total drive must exceed the total damping. The experimental observations of the mode seen during ICRF heating match all the characteristics expected of a TAE, hence that name is used here to refer to that mode. The mode observed during NBI has a toroidal mode number of  $n = 0$ , which means that it is not a TAE. However, its characteristics do match those of the so-called ‘Alfvén frequency mode’ (AFM) [19].

### 1.4. Related work

Experiments on TAEs, motivated by the issues mentioned in Section 1.1, were first performed with neutral beam plasmas in DIII-D [20–22] and TFTR [8, 9, 23]. Subsequent results have also come from the Princeton Beta Experiment — Modified (PBX-M) [24], JT-60U [25–27] and JET [28]. The results from JT-60U and JET concentrate predominantly on ICRF minority tail driven TAEs, although the JET work includes some results on neutral beam driven modes. Recent work on JET has included external excitation of the TAE by an antenna in order to measure directly the damping of the mode [29]. The results from DIII-D indicated that neutral beam ions were destabilizing TAEs with  $2 \leq n \leq 10$ , causing up to 70% loss of the beam ions which, in turn, caused

the beam ion beta to saturate. Losses were proportional to the TAE amplitude, and were largest near the midplane. Neutral beam ion driven TAEs were observed in TFTR at low  $B_T$ , with  $4 \leq n \leq 8$ . A loss of up to 50% of beam ions was inferred from the change in the neutron rate. In PBX-M, modes in the Alfvén frequency range were seen, localized near the  $q = 1$  surface, and having a ballooning character. The loss of beam ions due to the mode was inferred from a drop in the neutron rate during the mode. TAEs driven by H minority ICRF tail ions have been reported at JT-60U. The modes occurred with a threshold in power of  $\sim 3$  MW, were localized near the  $q = 1$  surface, and had  $4 \leq n \leq 12$ . The stored energy in the tail ion population was observed to drop by 20% during the TAEs. In JET, TAEs with  $n \leq 6$  were observed during combined NBI and ICRF heating. The TAE appeared above  $\sim 5$  MW of ICRF power, and resulted in a loss of beam ions that was linear with the mode amplitude.

The characteristics of the neutral beam driven AFM in TFTR and the losses produced by it are presented in Section 2 of this paper. Section 3 discusses some implications of these results. Section 4 describes the characteristics of losses from a TAE driven by hydrogen minority ICRF tail ions, while Section 5 draws implications from these results and Section 6 summarizes the paper.

## 2. NEUTRAL BEAM ION DRIVEN AFM

### 2.1. Mode characteristics

The NBI driven AFM in this experiment was observed under conditions of low toroidal field, with the injected 100 keV beam deuterons satisfying  $v_D \sim v_A$ , where  $v_D$  is the beam deuteron velocity. Typical parameters for these deuterium plasmas were:  $1 \text{ T} \leq B_T \leq 2 \text{ T}$ ,  $300 \text{ kA} \leq I_p \leq 700 \text{ kA}$ ,  $n_e = 3 \times 10^{19} \text{ m}^{-3}$ ,  $R = 2.40 \text{ m}$ ,  $a = 0.75 \text{ m}$ ,  $\beta_{\text{fast}} \sim 0.5\%$  and  $\langle \beta \rangle \sim 1\%$ . The mode was observed on the Mirnov coils, and had a frequency of approximately 120 kHz. The mode amplitude increased with increasing NBI power. During these shots, beam ion loss was observed with the 20° probe. The probe aperture was located between  $R = 3.41 \text{ m}$  (0.32 m from the plasma edge) and  $R = 3.51 \text{ m}$  (0.42 m from the plasma edge), with it most often being placed at  $R = 3.46 \text{ m}$  (0.37 m from the plasma edge). The limiter radius at the angular location of the probe was  $R = 3.525 \text{ m}$ .

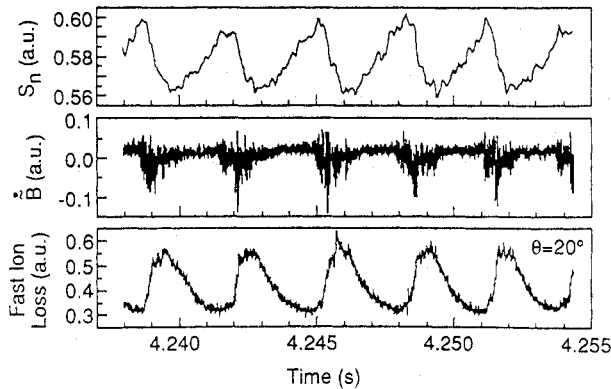


FIG. 1. Time histories of the neutron rate, the Mirnov coil signal and the rate of beam ion loss for a plasma in which an AFM was driven unstable by 100 keV deuterons from the neutral beam heating system of TFTR. For the shot shown (shot 60721),  $I_p = 420$  kA,  $B_T(0) = 1.47$  T and the other plasma parameters were as noted in Section 2. The probe aperture was located at  $R = 3.435$  m for this discharge.

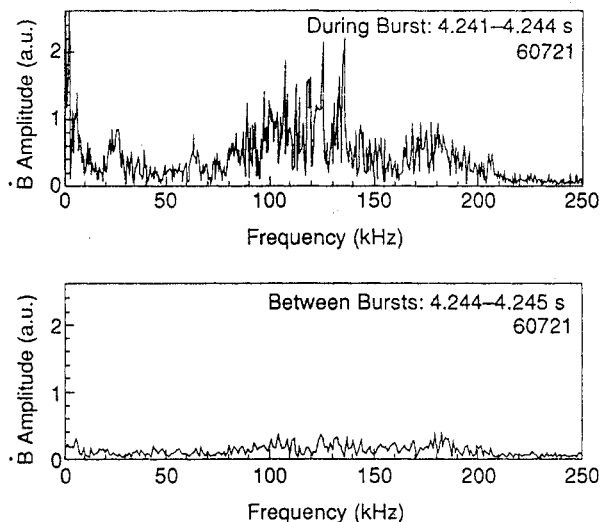


FIG. 2. Frequency spectra of the signal from a Mirnov coil during and between bursts of mode activity in the shot shown in Fig. 1.

Figure 1 shows the time histories of the neutron rate, a Mirnov coil signal and the rate of neutral beam ion loss to the  $20^\circ$  escaping alpha detector [23]. The bursts in the Mirnov signal are caused by the AFM. During each burst, the beam ion loss rate increases. The neutron rate is seen to drop during each burst, indicating an expulsion of beam ions. The time delay between the peak of the envelope of the Mirnov signal and the peak of the beam ion loss is about 0.5 ms. This interval corresponds to several tens of bounce

times for the trapped beam ions, and indicates that the loss mechanism requires numerous transits of the particle through the mode in order to cause expulsion. In this discharge, the bursts occur at a regular interval and result in approximately equal losses. There is a baseline loss rate to which the signal returns in between the bursts. This baseline loss is of trapped beam ions (see below) and probably results from the few per cent of beam neutrals that ionize at a sufficiently large minor radius to be born onto trapped orbits. Particles on those orbits are then lost due to stochastic toroidal field ripple diffusion.

Figure 2 compares the frequency spectrum of the Mirnov signal during a burst with the spectrum between bursts. The spectrum during a burst is centred around 120 kHz and is rather broad when compared with that of the TAE [8, 9]. Data from an array of Mirnov coils indicate that the toroidal mode number is  $n = 0$ . The dominant poloidal mode numbers are  $m = 1$  and  $m = 2$ , and the mode has a standing wave structure. The mode numbers were determined by fitting the phase data from a set of 30 Mirnov coils arranged at eight different toroidal angles. The coil arrays are described in more detail in Refs [30] and [31], and the fitting procedure is outlined in Ref. [10]. For these low  $m$ -numbers, the coil arrays are easily capable of measuring toroidal mode numbers of at least  $n = 4$ . No data are available on the radial structure of these modes.

## 2.2. Mode identification

The observation that this mode has  $n = 0$  implies that it is not a TAE. This mode might be an energetic particle mode (EPM) [32–34]. However, the observed  $n = 0$  mode structure does not match what would be expected theoretically for EPMS, namely modes with moderate or large  $n$ , since the growth rate of EPMS should be proportional to  $n$  [32, 34]. The  $n = 0$  standing wave structure and the broad frequency spectrum are typical of the AFM and lead us to identify this mode as an AFM [19]. The mode amplitude is also comparable to that seen in other AFMs. Recent theoretical work indicates that the AFM may be a global Alfvén eigenmode [35]. The empirically derived AFM frequency scaling predicts a mode frequency of  $\sim 130$  kHz for these plasmas, agreeing within the error bars with the observed frequency. By way of comparison, the TAE frequency computed with the central plasma parameters  $q = 1$  and  $B_T = 1.5$  T is 137 kHz. The only characteristic of the mode described here that does not match

those of previously observed AFMs is that it occurs in bursts; previous AFMs had a steady or slowly evolving amplitude. TAEs with  $4 \leq n \leq 8$  have been observed in TFTR under conditions very similar to these, as described in Refs [8] and [9]. The only difference between the parameters of the plasmas in this experiment and those described previously is in  $B_T$ , which was 1.5 T for most of the discharges described here, but was 1.0 T for the plasmas with TAEs in Ref. [8].

During the AFM bursts, there was also enhanced magnetohydrodynamic (MHD) activity at 25 kHz, and some at  $\sim 6$  kHz. The 6 kHz mode was observed in some shots to persist between the bursts, and therefore seems unlikely to be the cause of the bursting losses measured. This low frequency mode existed principally near the centre of the plasma, and appears to have had mode numbers  $n = 1$  and  $m = 1$ . The 25 kHz mode had  $n = 0$  according to the Mirnov coil array. In DIII-D, neutral beam driven TAEs were frequently accompanied by simultaneous fishbone modes at a lower frequency [20].

### 2.3. Correlation of loss rate to mode amplitudes

The characteristics of a group of 51 bursts taken from 12 nominally identical shots were compiled into a database. The quantities included in the database were the amplitudes of the two modes seen on the Mirnov coil signals, integrated over the duration of the burst, and two measures of the beam ion loss rate: (a) the change in the neutron rate during the burst (computed as in Ref. [17]) and (b) the estimated burst induced beam ion loss to the wall, based upon the signal to the  $20^\circ$  fast ion loss probe, integrated in time. The assumptions used to compute these estimates from the  $20^\circ$  probe data are described in Section 3. For this database, the amplitude of the AFM was defined as the increase in the Mirnov signal above the background levels for frequencies between 62.5 and 250 kHz, and the amplitude of the 25 kHz mode was defined as the increase above background levels of the Mirnov signal in the 10 to 62.5 kHz range. Of the 51 bursts, the AFM amplitude could be measured in all cases, the 25 kHz mode amplitude could be measured for 46 events, the change in the neutron rate could be measured in all cases, and the loss to the  $20^\circ$  probe could be measured for 23 events. From these quantities, an effort was made to determine statistically which mode was producing the beam ion loss and how that loss varied with mode amplitude.

Plots of various possible combinations of variables are shown in Fig. 3. Figure 3(a) depicts the change in neutron rate,  $\Delta S_n$ , plotted as a function of the AFM amplitude. Figure 3(b) shows  $\Delta S_n$  plotted against the 25 kHz mode amplitude. Figure 3(c) displays the loss to the  $20^\circ$  fast ion loss probe as a function of the AFM amplitude and Fig. 3(d) presents the loss to the  $20^\circ$  probe plotted against the 25 kHz mode amplitude. Finally, Fig. 3(e) depicts the amplitude of the 25 kHz mode, plotted against the AFM amplitude, showing the degree of correlation between the two modes.

Several possible relationships between the loss and the mode amplitude have been predicted by theories, depending upon the particular conditions of the instability and the fast ion velocity space. The predictions are that the loss will vary as  $\delta B^2$ , or  $\delta B^h$ , where  $0.5 \leq h \leq 1$  [36]. The quadratic dependence arises due to a diffusive process where non-resonant particles receive randomly phased perturbations of their orbits as they traverse the mode. A linear dependence results when particles interact coherently with the mode. However, as the particle's orbit, in drift orbit space, approaches the island induced by the mode, the dependence of the loss rate on mode amplitude varies smoothly from linear to square root [37].

In order to assess whether it is the AFM or the 25 kHz mode that drives the beam ion loss, both measures of loss were fitted to both mode amplitudes, using the functional form  $\Gamma = a \delta B^h$ , where  $\Gamma$  is a measure of the beam ion loss,  $\delta B$  is the mode amplitude and  $a$  and  $h$  are determined by a least squares fit. The results of this fit are shown in Table I, along with the correlation coefficient of the fit,  $h$ , and the number of points used,  $n$ . All of the fits exhibit good correlation coefficients, with the AFM amplitude fitting both loss measurements slightly better than the 25 kHz mode amplitude.

In order to try to quantify more completely the dependence of the loss upon the two mode amplitudes, a study of the goodness of the fits was made over restricted ranges of each  $\delta B$ . If the loss were due exclusively to one of these modes, then it would be expected that the least squares fit of the loss rate as a function of that mode's amplitude would still be good, even over this restricted range. It would also be expected that the coefficients found in the functional fitting would be close to those obtained when the whole dataset was fitted. However, if that mode were not producing the loss, then one might expect to see a lower goodness of fit and differing coefficients from the fit to the entire dataset. The two restricted

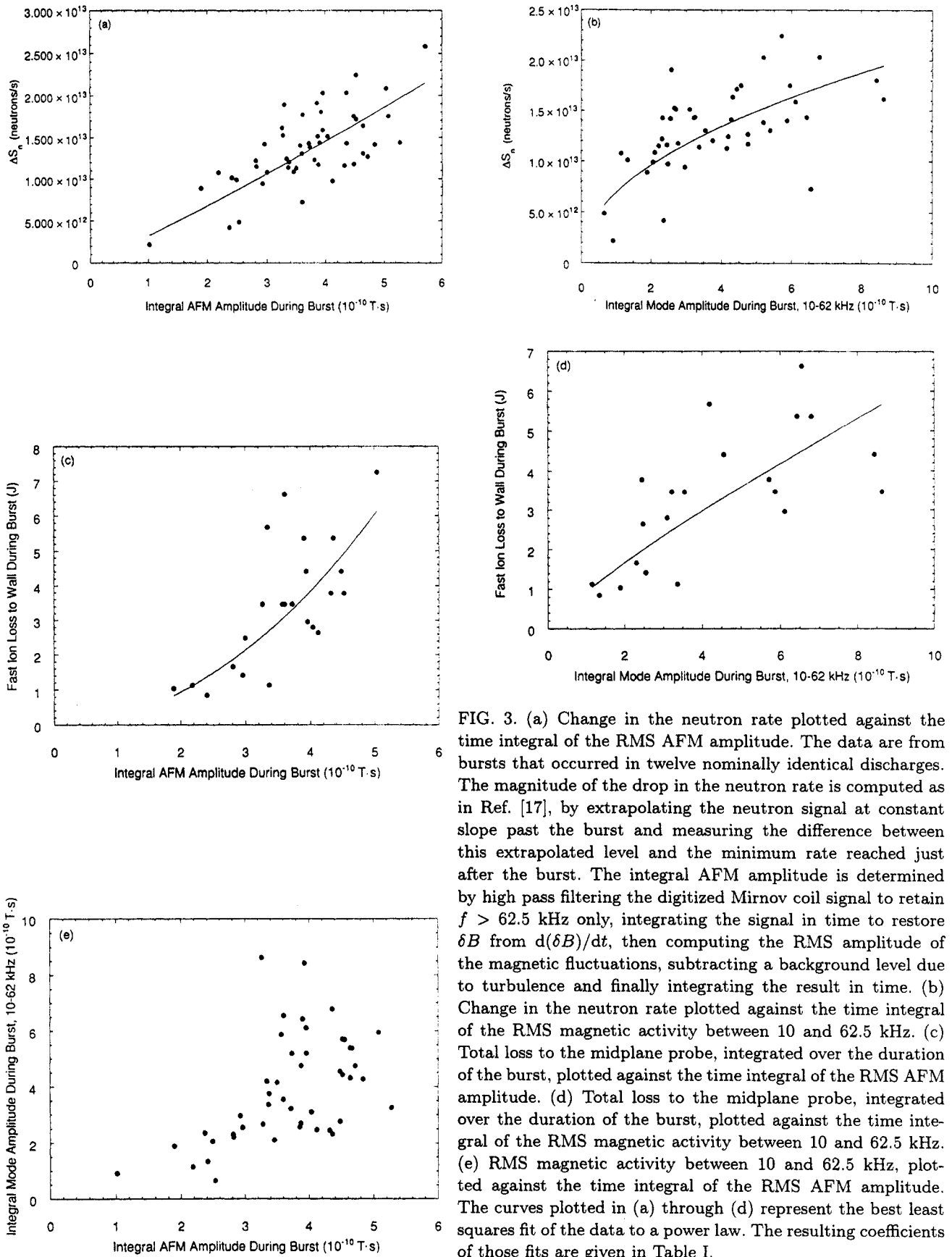


FIG. 3. (a) Change in the neutron rate plotted against the time integral of the RMS AFM amplitude. The data are from bursts that occurred in twelve nominally identical discharges. The magnitude of the drop in the neutron rate is computed as in Ref. [17], by extrapolating the neutron signal at constant slope past the burst and measuring the difference between this extrapolated level and the minimum rate reached just after the burst. The integral AFM amplitude is determined by high pass filtering the digitized Mirnov coil signal to retain  $f > 62.5$  kHz only, integrating the signal in time to restore  $\delta B$  from  $d(\delta B)/dt$ , then computing the RMS amplitude of the magnetic fluctuations, subtracting a background level due to turbulence and finally integrating the result in time. (b) Change in the neutron rate plotted against the time integral of the RMS magnetic activity between 10 and 62.5 kHz. (c) Total loss to the midplane probe, integrated over the duration of the burst, plotted against the time integral of the RMS AFM amplitude. (d) Total loss to the midplane probe, integrated over the duration of the burst, plotted against the time integral of the RMS magnetic activity between 10 and 62.5 kHz. (e) RMS magnetic activity between 10 and 62.5 kHz, plotted against the time integral of the RMS AFM amplitude. The curves plotted in (a) through (d) represent the best least squares fit of the data to a power law. The resulting coefficients of those fits are given in Table I.

ranges of mode amplitude were chosen to have the widest possible variation of the other mode's amplitude (Fig. 3(e)), in order to provide the best test of which mode explained the losses.

Table II presents the results when fits are made to points with integral AFM amplitude between  $3 \times 10^{-10}$  and  $4 \times 10^{-10}$  T·s. The points are fitted to the form  $\Gamma = c\delta B^k$ , and the values of  $h$  are from Table I, the fit to all points in the dataset. When the AFM amplitude is used as the independent variable, for both choices of the dependent variable, the fitted exponent changes less than when the 25 kHz mode amplitude is used. In fact, the exponent fitted when the 25 kHz amplitude is the independent variable and the change in neutron rate is the dependent variable is quite different from that quoted in Table I for the same fit. When the change in neutron rate is used as the dependent variable, the correlation coefficient is significantly higher for the fit to the AFM amplitude. When the 20° probe loss signal is the dependent variable, the fit to the 25 kHz mode amplitude has a slightly larger correlation coefficient.

Table III presents the results when fits are made to points with integral 25 kHz mode amplitude between  $2 \times 10^{-10}$  and  $3 \times 10^{-10}$  T·s. The points are fitted

to the form  $\Gamma = c\delta B^k$ , and the values of  $h$  are from Table I, the fit to all points in the dataset. Here, there were too few points with the 20° probe data (only four) to come to a useful statistical conclusion. However, if the change in neutron rate is used as a measure of beam ion loss, there is a significantly higher correlation with the amplitude of the AFM.

The statistical measure of the goodness of the fits over these limited ranges indicates that beam ion loss during the Mirnov bursts correlates significantly better with the AFM amplitude than with the 25 kHz mode amplitude.  $\Delta S_n$  fits best to essentially a linear function of the integral AFM amplitude, suggesting loss of beam ions by a coherent process. The integral loss to the 20° probe fits best to approximately the square of the integral AFM amplitude, suggesting loss by a diffusive process.

#### 2.4. Characteristics and orbits of the lost beam ions

The pitch angle distribution during the bursts did not change significantly from the distribution between bursts. Figure 4(a) compares the pitch angle distributions of the losses during and between

**Table I. Power Law Fits to Entire Beam Ion Loss Dataset**

$\delta B$	$\Gamma$	$a$	$h$	$R$	$n$
AFM	$\Delta S_n$	$3.20 \times 10^{12}$	1.09	0.693	45
25 kHz mode	$\Delta S_n$	$6.88 \times 10^{12}$	0.48	0.616	45
AFM	20° probe	0.230	2.03	0.704	23
25 kHz mode	20° probe	0.933	0.836	0.696	23

**Table II. Power Law Fits Over a Restricted Range in AFM Amplitude**

$\delta B$	$\Gamma$	$h$	$k$	$R$	$n$
AFM	$\Delta S_n$	1.09	0.96	0.339	23
25 kHz mode	$\Delta S_n$	0.48	0.046	0.122	23
AFM	20° probe	2.03	1.89	0.291	11
25 kHz mode	20° probe	0.836	0.58	0.340	10

**Table III. Power Law Fits Over a Restricted Range in 25 kHz Mode Amplitude**

$\delta B$	$\Gamma$	$h$	$k$	$R$	$n$
AFM	$\Delta S_n$	1.09	0.86	0.447	14
25 kHz mode	$\Delta S_n$	0.48	0.74	0.245	14

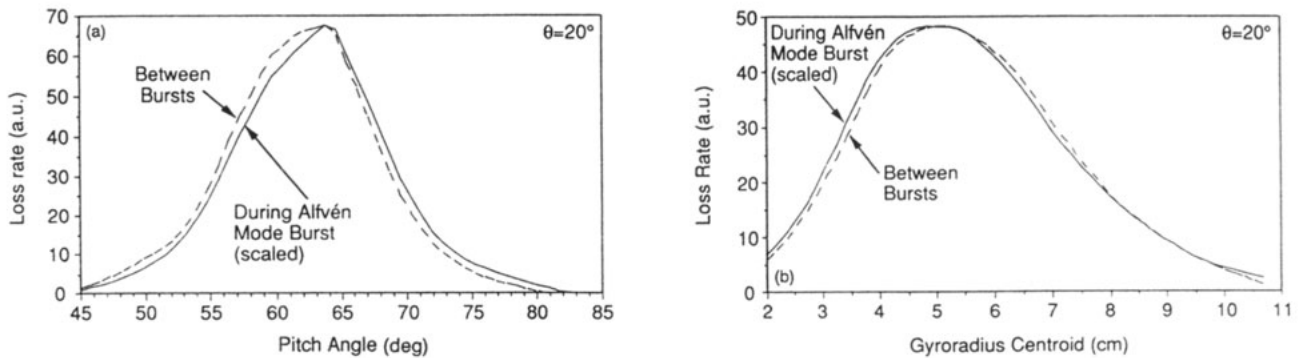


FIG. 4. (a) Detected pitch angle distributions of beam ion losses during and between bursts of TAE activity. The heights of the curves are rescaled to be equal for ease of comparison. A small increase in pitch angle is observed during the AFM burst, although during other bursts the pitch angle is sometimes seen to decrease. The boundary between passing and trapped particles for this discharge is at a pitch angle of  $47^\circ$ . (b) Detected distributions of gyroradii from the same times as in (a). The loss appears to shift very slightly to lower gyroradii during the mode. Again, the heights have been rescaled.

the bursts. In this figure, the amplitude of the distribution during the AFM burst is normalized to the amplitude of the distribution between the bursts to facilitate comparison. The pitch angles of the loss both during and between the bursts are similar. In this particular case, the loss during the burst shifts to higher pitch angles, i.e. to more deeply trapped particles, but this is not uniformly true. During some bursts in the same shot, the loss is at lower pitch angles. In this case, the loss peaks at a pitch angle of  $64^\circ$ , well into the trapped region of phase space. The pitch angle of the passing/trapped boundary is  $47^\circ$  at the  $20^\circ$  probe for these plasma conditions and particle energies. The typical shape of these orbits is depicted in Fig. 5.

The gyroradius distribution during the bursts does not change significantly from the distribution between the bursts. Figure 4(b) displays the gyroradius distributions (again normalized to the same amplitude) of the losses during and between the bursts. For the burst chosen, the same one as in Fig. 4(a), the particles lost during the burst are at slightly lower gyroradii. During other bursts, however, the gyroradius distribution does not change at all from that between the bursts. The gyroradius seen is that expected for birth energy (100 keV) deuterons.

The orbits of the particles lost lie in the stochastic ripple loss region. This is shown in Fig. 5, which depicts several orbits computed from the observed pitch angles and energies at the detector. These are for a 420 kA, 1.4 T plasma. Also shown in the figure

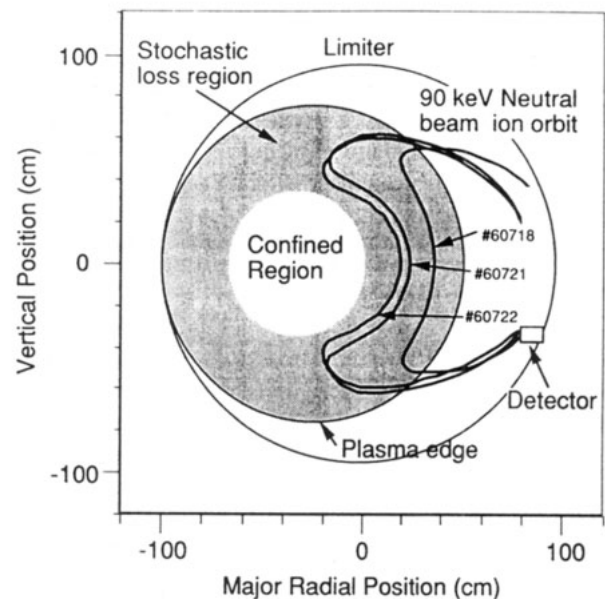


FIG. 5. Orbits computed from the observed pitch angles at the  $20^\circ$  detector at several different positions. All are banana orbits with their tips within the stochastic ripple domain, which is the darker shaded region in the plasma cross-section. The probe aperture positions were: shot 60 718,  $R = 3.49$  m; shot 60 721,  $R = 3.435$  m; and shot 60 722,  $R = 3.41$  m.

is the stochastic toroidal field ripple diffusion domain for 95 keV deuterons [38]. Any beam ion with banana tips in this domain is subject to stochastic ripple diffusion, which will eventually result in its loss to the wall near the midplane. As shown in this figure, the orbits of the lost particles detected at several probe

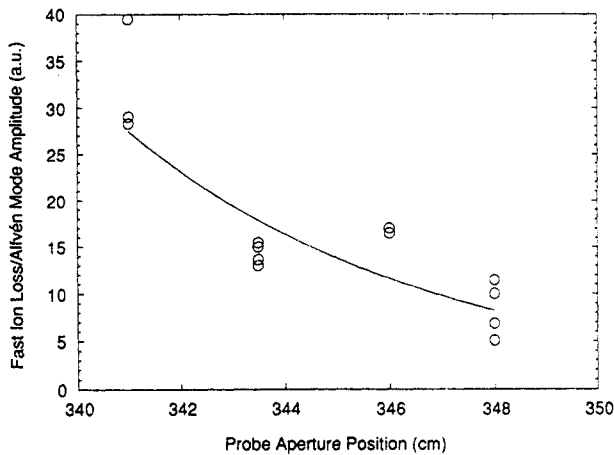


FIG. 6. Total beam ion loss to the  $20^\circ$  probe versus probe position. The limiter is at  $R = 352.5$  cm at this poloidal angle. The data show roughly an exponential scrape-off, with a characteristic length of  $\sim 6$  cm.

locations are all subject to stochastic ripple diffusion. Since essentially the same pitch angles are observed in the absence of the mode, the pitch angle data and this plot indicate that the losses in the absence of the mode can be attributed to stochastic ripple diffusion. The fact that additional loss driven by the mode appears at the same pitch angle suggests that the mode driven loss may result from a two step process in which the mode moves beam ions outward in minor radius until the particles are in the stochastic ripple domain. Ripple diffusion (either collisionless [38] or collisional [39]) then carries these particles out of the plasma. Since the ripple diffusion can take many bounces before the particle is ejected, this conjecture would be consistent with the observed time delay between the peak of the mode amplitude and the peak of the loss. Likewise, it would explain the fact, depicted in Fig. 1, that the losses persist for some time after the mode has vanished. It is also possible that stochastic diffusion can occur as the beam ions encounter an effective ripple in the field due to the magnetic fields of the mode itself (rather than due to the discreteness of the toroidal field coils). However, ripple diffusion in the mode's own fields would not explain the persistence of the loss after the mode has vanished.

Figure 6 shows the total loss to the probe versus position. The loss increases as the probe moves further inward away from the limiter, which is at  $R = 352.5$  m. Previous measurements of stochastic toroidal field ripple diffusion have found that the total loss of deuterium–deuterium (DD) and deuterium–

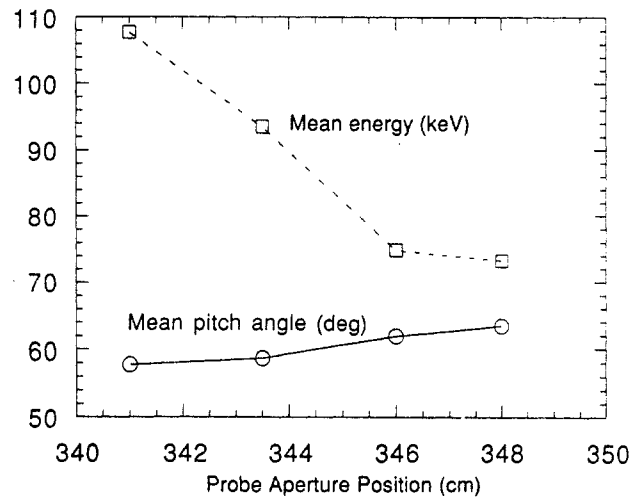


FIG. 7. Observed mean pitch angle and mean energy at the  $20^\circ$  detector versus probe position, for AFM driven neutral beam ion loss.

tritium (DT) fusion products versus probe position has an exponential form [5]. If the data in Fig. 6 are fitted to an exponential function, the result is an e-folding distance of  $\sim 6$  cm.

Figure 7 depicts the mean pitch angle and the mean observed energy of the lost deuterons as a function of probe position. The mean pitch angle varies by  $\sim 5.7^\circ$  over the 7 cm that the probe is scanned. The mean energy varies from about 73 to 107 keV, depending upon position. The observed decrease in energy as the probe moves away from the plasma cannot be attributed to collisional slowing down, as this proceeds too slowly: the losses at all positions change on the same time-scales, as depicted in Fig. 1. However, this variation of energy with position would be consistent with outward major radial transport of beam ions as they interact with the mode, as outlined in Section 5. Ions that interacted with the mode at greater length would lose more energy to it, but would also be transported to larger major radii where they would experience a larger toroidal field ripple and scrape-off further into the limiter shadow.

### 3. DISCUSSION OF NBI LOSS RESULTS

#### 3.1. Relationship of loss rate to mode amplitude

The regular bursting behaviour depicted in Fig. 1 is consistent with a cyclical process in which beam injection increases the population of fast ions up to a point above the instability threshold, whereupon

the instability sets in, ejects the fast ions, and falls below threshold [40]. In contrast to the cases studied in Ref. [19], the AFMs here appear to be driven by the neutral beam ions. This is the first case known in which fast ion losses result from AFMs. The low plasma current in the discharges studied here may be the reason, since it allows fast ions to have a larger orbit width and, thus, a greater chance of interacting with the AFM. Ordinarily, the AFM is edge localized.

Owing to their relatively low density, the neutron production in the discharges considered here is predominantly (80% according to the SNAP transport code [41]) from reactions of beam ions with other beam ions, i.e.  $S_n \propto n_f^2$ , where  $n_f$  is the fast ion density. In contrast, the neutron production in the DIII-D experiments was computed to be dominantly from beam-plasma reactions [20]. Each individual burst of the AFM produces a reduction in the neutron rate of between 5 and 10%, so that the change in beam ion density can be treated perturbatively:  $S_n \propto n_f^2 = n_{f0}^2(1 - \Delta n_f/n_{f0})^2$ . (This zero dimensional model ignores the radial dependence of the fast ion density.) The result is that the change in the neutron rate, to lowest order, is linear in the change in the beam ion density:  $\Delta S_n \propto -2n_{f0}\Delta n_f$ . This means that the change in neutron rate, the vertical axis in Fig. 3(a), can be regarded as directly proportional to the change in the beam ion density, i.e. the amount of loss. Thus, the fact that the best fit to the data in Fig. 3(a) is nearly linear implies that the fast ion loss is approximately linearly proportional to the AFM amplitude.

Although the neutron data imply that the fast ion loss is linearly proportional to the AFM amplitude, the direct measurements of loss from the 20° probe seem best fitted by approximately the square of the mode amplitude. The neutron data constitute a more global measurement of the change in the fast ion population, since they account for fast ions at all pitch angles and minor radii. In contrast, the 20° probe measurement of the loss is limited to trapped ions near the edge. The reason for this difference between loss measures in their functional dependence on the mode amplitude is not clear. Ions lost to the 20° probe may arise from pitch angle scattering due to interaction with the mode. This would be a non-resonant, diffusive process, resulting in a quadratic dependence upon the mode amplitude, as seen. Such a pitch angle scattering process would also explain the presence of a population of trapped beam ions, which is otherwise present only in small amounts from collisional pitch angle scattering. The pitch angle

scattered ions are lost through the stochastic toroidal field ripple diffusion process, as noted in the discussion about Fig. 5 in Section 2.4. Again, because they account for fast ions at all pitch angles, not just purely trapped ions, the neutron rate data are the most reliable measure of the beam ion loss, and they indicate that loss is a linear function of mode amplitude. A similar linear dependence of fast ion loss on mode amplitude has also been observed in JET [28].

Because the AFM and 25 kHz modes occur together, it is conceivable that the beam ion losses result from the combined effects of the two modes. However, the data in Tables II and III tend to contradict this hypothesis. If the loss were due to the combined effect of the modes, fitting to the loss data over a restricted range of amplitudes of one mode should improve the correlation between the loss and the amplitude of the other mode. However, just the reverse is seen: the correlation coefficient diminishes.

### 3.2. Absolute loss level

It is possible to cross-calibrate the 20° detector from the 90° detector under other quiescent discharge conditions where fusion product loss dominates [5]. Assuming the scintillator response is linear with the fast ion power incident upon it, that calibration can be used for neutral beam losses as well. For a typical discharge with a bursting frequency as shown in Fig. 1, the AFM bursts result in losses to the wall of  $\sim 0.06$  W/cm<sup>2</sup>. Knowing that these losses result from stochastic toroidal field ripple diffusion, the total loss can be crudely estimated by assuming this loss rate holds between 0 and 30° below the outboard midplane, and is axisymmetric. The result is that total losses are estimated to be  $\sim 6$  kW, or  $\sim 0.06\%$  of the injected power of 10 MW. This result is not consistent with the change in the neutron rate produced by the bursts, which indicates  $\sim 10\%$  beam ion loss. There are several assumptions used in these estimates that may be erroneous. First, the loss rate inferred from the change in the neutron rate assumes that the particles have actually been lost from the plasma, when they may only have been displaced to some region where they produce fewer neutrons. Second, the loss rate inferred from the probe is based on an assumption about the poloidal distribution of the loss, which may be quite different from the actual distribution. Finally, the probe used cannot detect particles with pitch angles below 40°, which may lead to an underestimate of the losses if particles in this pitch angle range are lost in quantity. In fact, most

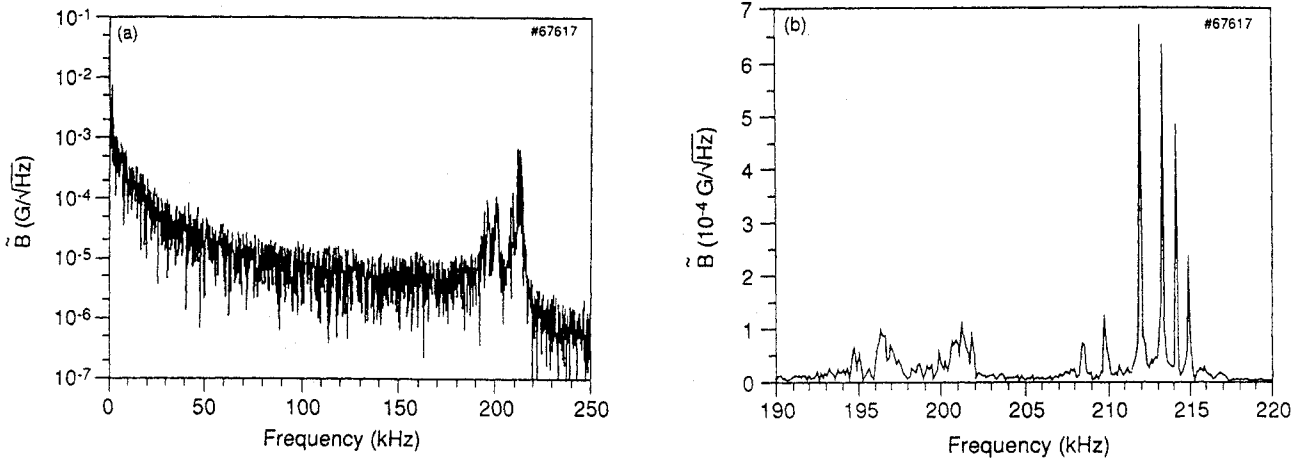


FIG. 8. (a) Frequency spectrum of magnetic fluctuations measured by a Mirnov coil during an ICRF hydrogen minority tail driven TAE (shot 67617,  $I_p = 1.8$  MA,  $R = 2.625$  m,  $a = 0.99$  m,  $B_T = 3.3$  T and  $P_{RF} = 8.3$  MW). (b) The same frequency spectrum, plotted over a narrower range of frequency to show the multiple modes present.

of the beam ions in the plasma do lie below this cut-off in pitch angle. Measurements in DIII-D indicated much higher beam ion loss powers than this power inferred from the probe measurement [20].

The essentially linear dependence of the loss upon the AFM amplitude indicates a coherent interaction between the fast ions and the mode which, in this case, transports the ions into the stochastic ripple loss domain. A similar case of TAE transport of particles into the ripple trapping loss domain has been studied numerically, and simulations show the same characteristic linear relationship between the mode amplitude and the fast ion loss rate [42]. Because the loss is not diffusive, we have not sought to estimate a fast ion diffusion coefficient.

#### 4. HYDROGEN MINORITY ICRF TAIL DRIVEN TAEs

##### 4.1. Mode characteristics

Another condition in TFTR in which Alfvén modes were driven is during hydrogen minority ICRF heating [10–16]. In such plasmas, the tail ions can exceed the Alfvén velocity and drive TAEs. Typical  $^4\text{He}$  or deuterium plasma parameters were:  $B_T = 3.4$  T,  $1.3 \text{ MA} \leq I_p \leq 1.8$  MA,  $R = 2.62$  m,  $a = 0.98$  m,  $\langle n_e \rangle = 2.5 \times 10^{19} \text{ m}^{-3}$ ,  $3 \text{ MW} \leq P_{ICRF} \leq$

$11 \text{ MW}$ ,  $f_{RF} = 47 \text{ MHz}$ ,  $T_{\text{tail}} = 300\text{--}600 \text{ keV}$  ( $v_{\text{tail}} \sim v_A \sim 1 \times 10^7 \text{ m/s}$ ),  $\langle \beta \rangle = 0.3\%$  and  $\langle \beta_{\text{fast}} \rangle = 0.03\%$ .

Under these conditions, TAEs appeared as magnetic fluctuations at frequencies between 170 and 250 kHz. Figures 8(a) and (b) show typical frequency spectra for such a mode, which often included several modes very closely spaced in frequency. The modes were also seen with the microwave reflectometer [11] and appeared only when the ICRF power exceeded 3 MW (equivalently, when the fast ion tail stored energy exceeded  $\sim 70$  kJ). The mode frequency scales inversely with the square root of plasma density, in agreement with the equation for the Alfvén frequency. Its scaling with magnetic field could not be checked convincingly since changing  $B_T$  also alters the ICRF resonance location. Similar behaviours of mode onset and frequency scaling have also been observed during minority ICRF heating in JET and JT-60U [25–28].

It was not possible to measure the mode numbers directly for the TAEs discussed in this section, as the Mirnov coil system was not suitably arranged. Because of the combination of  $m$ -numbers within a single- $n$  TAE, measurements of  $n$  can only be made reliably by comparing signals from an array of Mirnov coils all located at exactly the same poloidal angle, but distributed in toroidal angle. In later TFTR campaigns, where the array was reconfigured to allow measurement of the mode numbers of TAEs [10], similar discharges typically had modes with  $4 \leq n \leq 10$ .

#### 4.2. Global characteristics of the loss

Hydrogen minority tail ion losses resulted from the TAEs. These were most easily measured by the 45 and 60° probes, which are in fixed locations and are better protected from the plasma heat flux than is the 20° probe. Figure 9 displays the time history of a

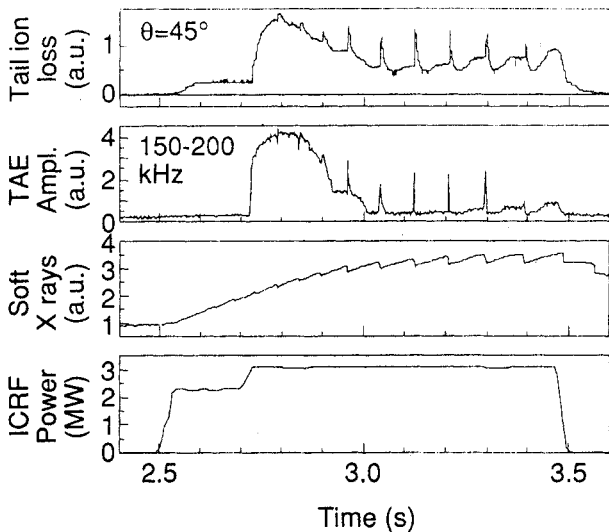


FIG. 9. Time history of a discharge with hydrogen minority ICRF tail ion driven TAE including: tail ion loss rate at the 45° escaping alpha detector, TAE amplitude from a Mirnov coil, soft X ray signal showing the sawtooth behaviour of the discharge and applied ICRF power.

discharge that contained TAEs driven by the hydrogen minority tail ions. The top trace depicts the total fast ion loss to the 45° escaping alpha probe versus time. The second trace is the summed RMS amplitude of all modes within the range from 150 to 200 kHz. When the mode appears, the fast ion loss is seen to increase suddenly and substantially. As time progresses, the mode amplitudes diminish, as do the fast ion losses. This, presumably, is due to some evolution of the tail ion distribution. A similar behaviour has been observed in JET [28]. At the sawtooth crashes (seen in the third trace) the modes momentarily turn on again, and the losses increase correspondingly. This, it is postulated, is due to a rearrangement of the fast ion profile. This figure also shows the turn-on threshold of 3 MW. The tail ions that are lost are trapped ions whose energies lie in the range 0.5 to 1 MeV, on the basis of the gyroradii detected. The lower end of this range, 0.5 MeV, is very close to the lower cut-off energy of the probes and it corresponds to protons whose velocities are approximately equal to the Alfvén velocity.

Figure 10(a) depicts the total RMS amplitude of the modes present, as determined from the Mirnov coils, and the escaping tail ion loss power as functions of the applied ICRF power. Both quantities increase approximately linearly with the applied ICRF power (more easily seen in Fig. 10(b)). The escaping tail ion loss power can be estimated assuming that the poloidal distribution of the losses is the same as that

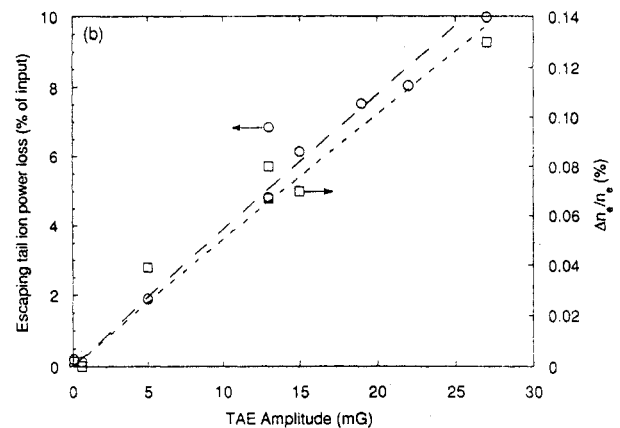
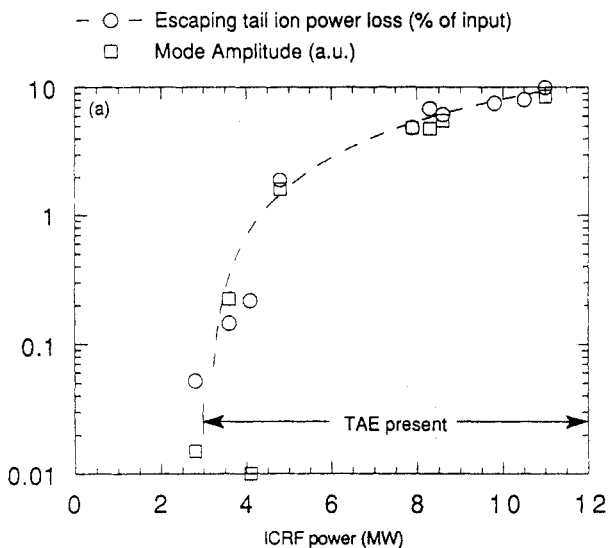


FIG. 10. (a) TAE amplitude and escaping tail ion loss power versus applied ICRF power. (b) Escaping tail ion loss power and density fluctuation level as measured by a microwave reflectometer versus the mode amplitude measured by the Mirnov coils (shots 67 611 to 67 631). In both plots, each unit for the escaping ion loss rate is approximately 1% of the input power, within the errors of calibration described in the text.

of first orbit loss. This assumption is known to be incorrect, since tail ion losses at the 90° detector position are negligible, while first orbit loss there is not. However, it provides the only available absolute calibration of the 45° detector. Comparison of the fast ion loss signal in the 45° detector during the TAEs to the DD fusion product loss signal during an ordinary neutral beam heated shot yields an absolute magnitude for the losses produced by the TAE. Because of the number of assumptions in this process, the uncertainties in the power loss are accurate only to within an order of magnitude. Setting aside these uncertainties, it is apparent that a significant amount of power is lost in ICRF tail ions when the TAE amplitude is large. In the worst case shown, with 11 MW of applied ICRF power, an estimated 1 MW is lost due to escaping tail ions.

This substantial loss may help explain two other experimental observations. First, it is seen that the energy stored in fast ions does not increase with ICRF power for powers above 5 MW in <sup>4</sup>He majority plasmas [12]. It may be that part or all of this additional input power is rapidly lost to the walls in tail ions (the uncertainty of the measurements described above does not preclude the possibility that all the additional input power above 5 MW is lost in escaping tail ions). Secondly, some in-vessel components in TFTR that lie ~ 10 cm in the shadow of the limiters have been melted or damaged due to excessive heating. This damage is concentrated near the midplane and corresponds to where most of the tail ions should be lost due to the TAE, as described below.

Figure 10(b) depicts the same data as in Fig. 10(a), but plotted as power loss versus total RMS mode amplitude. The relationship between the two quantities is best fitted by a straight line. This is consistent with the relationship between mode amplitude and losses seen in the NBI driven case described above. This linearity is again in agreement with reported JET results [28].

#### 4.3. Characteristics and orbits of the lost tail ions

The loss versus poloidal position of the probes is plotted in Fig. 11, and shows that the losses increase rapidly towards the midplane. Unfortunately, the 20° detector is of a different geometry than the others, with its aperture 3 cm behind the probe tip, rather than 1 cm as for the others. This difference makes it difficult to compare the fluxes in each probe directly. This poloidal distribution is consistent with a loss

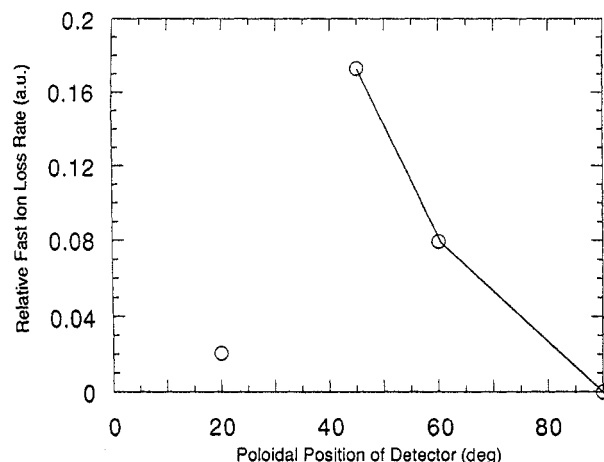


FIG. 11. TAE induced loss of tail ions versus poloidal angle (shot 67043).

process that causes a finite sized radial step within one bounce time.

Figure 12 shows the orbits of particles that enter the 20, 45 and 60° detectors with and without the TAEs (the 90° detector sees a negligible signal). The ICRF resonance layer is shown as a vertical dashed line in each figure. In the cases of the 45 and 60° detectors, it can be seen that the TAEs cause the pitch angle of the observed loss to increase, i.e. more deeply trapped particles are lost. This was also sometimes observed with the NBI driven AFMs (Fig. 4(a)). For the 20° detector, the loss in the absence of the TAEs was too small to detect, hence no orbit is plotted for that case. However, during the TAEs, a significant loss is observed, with a typical orbit as depicted in Fig. 12(c). The intriguing feature of these data is that particles which must have originated at the ICRF resonance layer now occupy orbits which are far removed from that region. The orbit has been displaced radially from the hydrogen cyclotron layer in Fig. 12(c) by about 0.8 m, and this motion occurs in less than a tail ion slowing down time, which is ~ 200 ms. This rate of transport is considerably larger than that observed for spatial diffusion of fast ions in quiescent plasmas, which typically occurs with a diffusion coefficient of the order of 0.1 m<sup>2</sup>/s [43].

Figure 13 displays the peak pitch angle of the tail ion loss during the TAE as a function of the plasma current. For both the 45 and 60° detectors, the peak pitch angle diminishes as the plasma current increases. This may indicate something about the nature of the loss, but is also consistent with fact that the banana widths will be reduced as the plasma current increases, so that a particle will have to have a

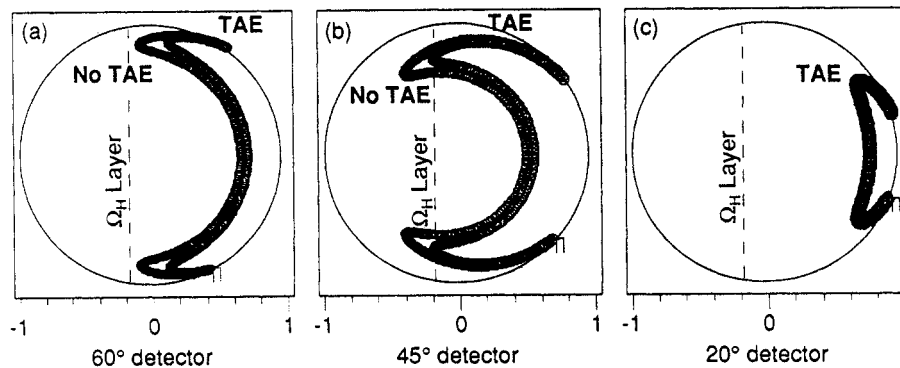


FIG. 12. (a) Escaping ICRF tail ion orbits with and without the TAE, as observed at the 60° detector. (b) Escaping ICRF tail ion orbits with and without the TAE, as observed at the 45° detector. (c) Escaping ICRF tail ion orbit during the TAE only, as observed at the 20° detector. The dashed line labelled ' $\Omega_H$  layer' indicates the position of the fundamental hydrogen cyclotron resonance in the plasma cross-section.

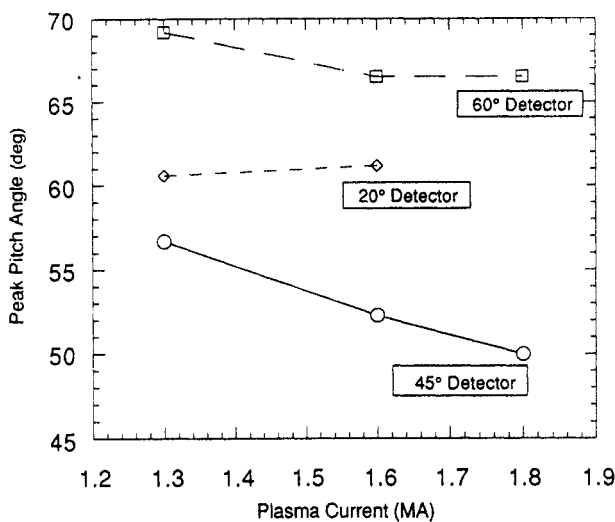


FIG. 13. Peak pitch angle of the TAE induced tail ion loss in several detectors as a function of plasma current (shots 67 011, 67 043, 67 612 and 68 752).

lower pitch angle to reach the detector position. The peak pitch angle observed in the 20° detector does not change over the range observed.

Finally, Fig. 14 indicates the variation with applied ICRF power of the peak pitch angles and energies observed in the 45 and 60° detectors. The two detectors display contrasting behaviours: in the 45° detector, the peak energy and the peak pitch angle of the particle losses are both observed to increase as the

ICRF power is increased. However, the data from the 60° detector reveal a constant pitch angle and energy over the entire range of ICRF power. It is unclear why the data from these two detectors, which otherwise tend to express similar trends, are so different in this instance.

## 5. DISCUSSION OF HYDROGEN MINORITY ICRF RESULTS

The ICRF minority tail driven TAE does not exhibit a bursting character like the neutral beam driven AFM discussed in Sections 2 and 3, but instead occurs steadily, with slow changes in mode amplitude. This difference in behaviour may arise from the difference in the way the fast ion population is created. In the ICRF case, fast ions are accelerated from the bulk ion distribution and must cross, in a continuous fashion, the threshold for excitation of the TAE. In the NBI case, ions are injected at an energy well above threshold. Additionally, the plasma current in the neutral beam plasmas described above was quite low, such that a small mode could result in a large loss of fast ions from the plasma. With the higher plasma current in the ICRF case, the mean radial displacement of the fast ions could be substantially smaller for the same mode amplitude, resulting in a smaller change in the instability driving term.

The linear relationship between the TAE amplitude and the loss rate suggests that the loss is due to

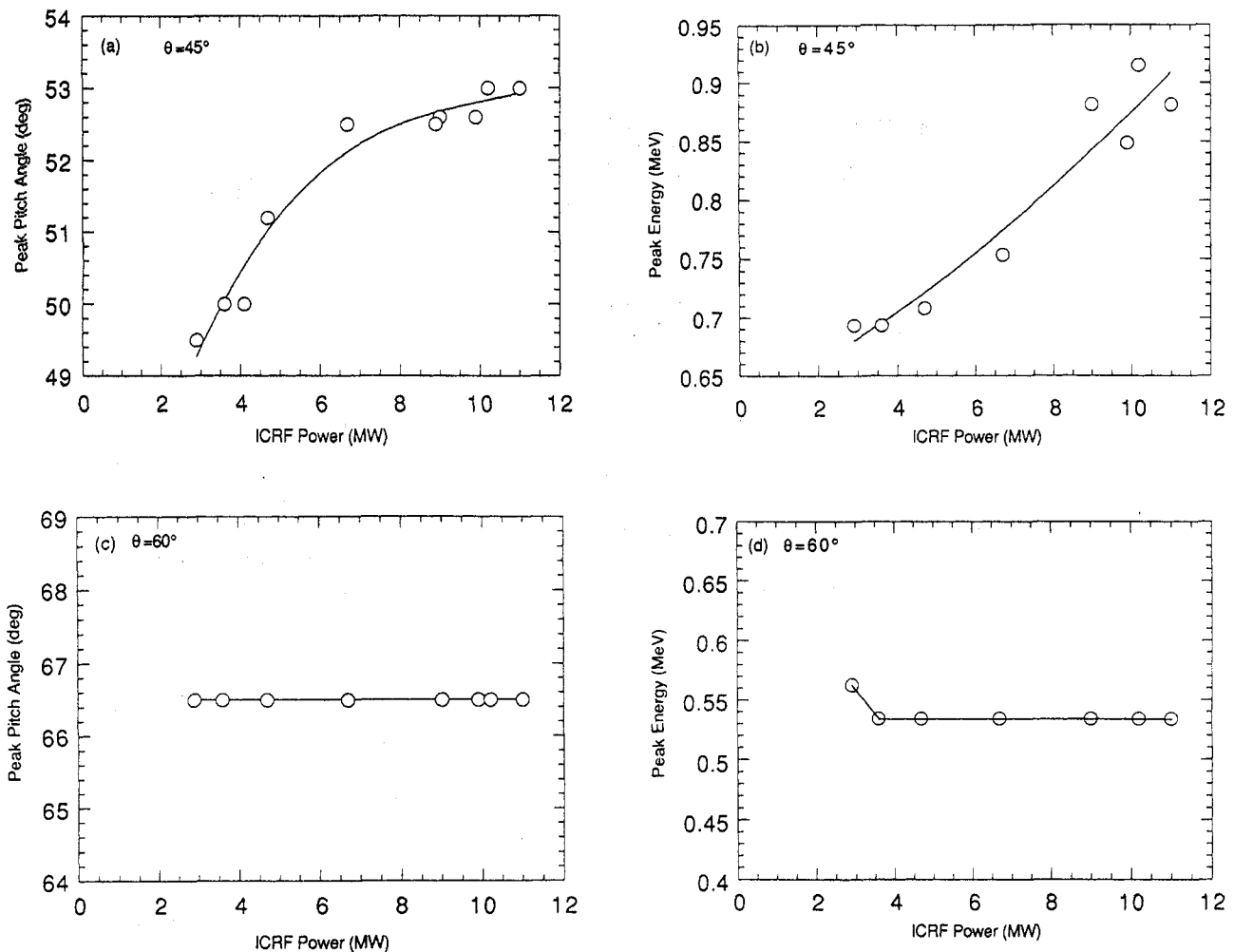


FIG. 14. (a) Peak pitch angle of the TAE induced hydrogen minority tail ion loss in the  $45^\circ$  detector plotted versus applied ICRF power. For the sake of comparison, the passing/trapped boundary (fattest banana orbit) for 0.8 MeV proton orbits reaching this detector is at a pitch angle of  $46^\circ$ . (b) Peak energy of the TAE induced hydrogen minority tail ion loss in the  $45^\circ$  detector plotted versus applied ICRF power. (c) Peak pitch angle of the TAE induced hydrogen minority tail ion loss in the  $60^\circ$  detector plotted versus applied ICRF power. For the sake of comparison, the passing/trapped boundary (fattest banana orbit) for 0.5 MeV protons reaching this detector is at a pitch angle of  $46^\circ$ . (d) Peak energy of the TAE induced hydrogen minority tail ion loss in the  $60^\circ$  detector plotted versus applied ICRF power. For these shots, the parameters were:  $I_p = 1.8$  MA,  $R = 2.625$  m,  $a = 0.99$  m,  $B_T = 3.3$  T and  $P_{RF} = 2.9$ –11 MW (shots 67611 to 67631).

a process that is coherent in nature, rather than diffusive. Observations from the DIII-D and JET tokamaks also indicate a linear relationship between the TAE amplitude and the particle loss rate [20–22]. Computational models of alpha loss for the Compact Ignition Tokamak (CIT) [36] predict loss of a coherent character at first, followed by loss of a diffusive nature (loss rate quadratic in mode amplitude) as the most easily lost particles are depleted. This computation may not apply well to this experiment since the parameters used differ significantly from

those in the experiment. In particular, the present experiments do not contain an isotropic distribution of fast ions, but one that is dominated by trapped ions. In addition, in the experiment, there is a continual source of new fast ions accelerated by the ICRF waves, while in the simulation there is a population that is depleted and not replenished with time.

A loss mechanism which is consistent with the observation that more deeply trapped tail ions are lost during the TAE is this: the TAE causes transport of resonant fast ions outward in major radius.

Since the bounce frequency of the particles is roughly equal to the TAE frequency, this is possible from the point of view of destroying the conservation of a particle's canonical toroidal angular momentum. The 20° detector data seem especially to support this interpretation, since the tail ions appear radially outward from where they are created, and are moved a substantial distance (several banana widths) to the detector within a fraction of a slowing down time. This might also explain the observed linear relationship between loss rate and mode amplitude. A similar mechanism was previously found to be responsible for the expulsion of neutral beam ions during fishbone oscillations [44]. TAEs result in exactly this type of radial motion in numerical models of the transport of ICRF minority tail ions into the ripple loss cone in TFTR [42].

## 6. SUMMARY

In summary, AFMs in TFTR driven by NBI ions and TAEs driven by hydrogen minority ICRF tail ions produced fast ion losses. The AFMs were identified in the beam injected plasmas by their  $n = 0$ ,  $m = 1$  or  $m = 2$  mode structure, their standing wave mode structure and their broad frequency spectrum. Several aspects of the loss of neutral beam ions due to the AFM appear to result from the mode moving those ions into the stochastic toroidal field ripple loss region of the plasma. For this case, the fast ion power measured in the loss detectors is a negligible fraction of the total applied power.

ICRF tail ion driven TAEs are also observed in TFTR, typically with multiple  $n$ -numbers present. The TAEs cause losses of tail ions in detectors at 20, 45, and 60° below the outer midplane of TFTR, but not at 90°. In the worst cases, fast ion losses totalling of the order of tens of per cent of the applied power are observed. There is clear evidence of mode induced transport of the lost tail ions to larger major radii, which is also supported by numerical modelling. In both the AFM and TAE cases, the magnitude of the losses varies linearly with the amplitude of the mode, indicating that a coherent interaction between the particles and the modes is driving the losses.

Further work in the area of TAE induced fast ion losses could include calculation of particle losses from TFTR plasmas, with the focus on identifying the classes of particles lost and the processes that result in the observed characteristics of the loss reported here. Additional experimental work with diagnostics

of confined fast ions could be used to verify the accuracy of the models for the driving terms for both passing and trapped particles, as well as the strength of the 'sideband' drive at  $v_f \sim v_A/3$ . The issue of alpha particle driven TAEs and the resulting alpha losses is being studied in TFTR's DT experiments.

## ACKNOWLEDGEMENTS

This work was supported by USDOE Contract No. DE-AC02-76-CHO-3073. The support of Drs R. Hawryluk and K. McGuire is appreciated.

## REFERENCES

- [1] PUTVINSKI, S., et al., in Plasma Physics and Controlled Nuclear Fusion Research 1994 (Proc. 15th Int. Conf. Seville, 1994), Vol. 2, IAEA, Vienna (1995) 535.
- [2] ZWEBEN, S.J., Nucl. Fusion **29** (1989) 825.
- [3] ZWEBEN, S.J., et al., Nucl. Fusion **30** (1990) 1551.
- [4] ZWEBEN, S.J., et al., Phys. Fluids B **2** (1990) 1411.
- [5] BOIVIN, R.L., Measurements of Charged Fusion Product Diffusion in TFTR, PhD Thesis, Princeton Univ., NJ (1991).  
BOIVIN, R.L., ZWEBEN, S.J., WHITE, R.B., Nucl. Fusion **33** (1993) 449.
- [6] ZWEBEN, S.J., et al., Nucl. Fusion **35** (1995) 893.
- [7] TOBITA, K., et al., Nucl. Fusion **34** (1994) 1097.
- [8] WONG, K.-L., et al., Phys. Rev. Lett. **66** (1991) 1874.
- [9] WONG, K.-L., et al., Phys. Fluids B **4** (1992) 2122.
- [10] FREDRICKSON, E.D., MCGUIRE, K.M., CHANG, Z.Y., Rev. Sci. Instrum. **66** (1995) 813.
- [11] WILSON, J.R., et al., in Plasma Physics and Controlled Nuclear Fusion Research 1992 (Proc. 14th Int. Conf. Würzburg, 1992), Vol. 1, IAEA, Vienna (1993) 661.
- [12] PHILLIPS, C.K., et al., in Radio Frequency Power in Plasmas (Proc. 10th Top. Conf. Boston, 1993), AIP, New York (1994) 44.
- [13] TAYLOR, G., et al., Phys. Fluids B **5** (1993) 2437.
- [14] FREDRICKSON, E.D., et al., Nucl. Fusion **35** (1995) 1457.
- [15] WONG, K.L., et al., in Radio Frequency Power in Plasmas (Proc. 10th Top. Conf. Boston, 1993), AIP, New York (1994) 409.
- [16] WONG, K.L., et al., Phys. Rev. Lett. **76** (1996) 2286.
- [17] BOIVIN, R.L., KILPATRICK, S., MANOS, D., ZWEBEN, S.J., Rev. Sci. Instrum. **61** (1990) 3208.
- [18] DARROW, D.S., et al., Rev. Sci. Instrum. **66** (1995) 476.
- [19] CHANG, Z., et al., Nucl. Fusion **35** (1995) 1469.
- [20] DUONG, H., et al., Nucl. Fusion **33** (1993) 749.

- [21] HEIDBRINK, W.W., et al., Nucl. Fusion **31** (1991) 1635.
  - [22] STRAIT, E.J., et al., Nucl. Fusion **33** (1993) 1849.
  - [23] DARROW, D.S., et al., in 1992 International Conference on Plasma Physics (Proc. Conf. Innsbruck, 1992), Vol. 16C, Part I, European Physical Society, Geneva (1992) 431.
  - [24] SESNIC, S., et al., Nucl. Fusion **33** (1993) 1877.
  - [25] KIMURA, H., et al., Phys. Lett. A **199** (1995) 86.
  - [26] SAIGUSA, M., et al., Plasma Phys. Control. Fusion **37** (1995) 295.
  - [27] KIMURA, H., et al., Jap. J. Plasma Fusion Res. **71** (1995) 1147.
  - [28] ALI-ARSHAD, S., CAMPBELL, D.J., Plasma Phys. Control. Fusion **37** (1995) 715.
  - [29] FASOLI, A., et al., Phys. Rev. Lett. **75** (1995) 645.  
FASOLI, A., et al., Nucl. Fusion **35** (1995) 1485.
  - [30] FREDRICKSON, E.D., COLCHIN, R., McGUIRE, K., MORRIS, W., SAUTHOFF, N., Rev. Sci. Instrum. **57** (1986) 2084.
  - [31] FREDRICKSON, E.D., et al., Rev. Sci. Instrum. **59** (1988) 1797.
  - [32] CHEN, L., Phys. Plasmas **1** (1994) 1519.
  - [33] ZONCA, F., CHEN, Liu, Phys. Plasmas **3** (1996) 323.
  - [34] SANTORO, R.A., CHEN, Liu, Phys. Plasmas **3** (1996) 2349.
  - [35] VILLARD, L., VACLAVIK, J., Nucl. Fusion **37** (1997) 351.
  - [36] SIGMAR, D.J., et al., Phys. Fluids B **4** (1992) 1506.
  - [37] WU, Yanlin, et al., Phys. Plasmas **2** (1995) 4555.
  - [38] GOLDSTON, R.J., WHITE, R.B., BOOZER, A.H., Phys. Rev. Lett. **47** (1981) 647.
  - [39] REDI, M.H., et al., Nucl. Fusion **35** (1995) 1191.
  - [40] HEIDBRINK, W.W., et al., Phys. Fluids B **5** (1993) 2176 .
  - [41] TOWNER, H.H., et al., Rev. Sci. Instrum. **63** (1992) 4753.
  - [42] WHITE, R.B., et al., Phys. Plasmas **2** (1995) 2871.
  - [43] HEIDBRINK, W.W., SADLER, G.J., Nucl. Fusion **34** (1994) 535.
  - [44] WHITE, R.B., et al., Phys. Fluids **26** (1983) 2958.
- (Manuscript received 2 February 1996  
Final manuscript accepted 18 March 1997)
- (E-mail address of D.S. Darrow: ddarrow@pppl.gov)